remote sensing

MDPI

Communication

Frequency Increment Design Method of MR-FDA-MIMO Radar for Interference Suppression

Zhixia Wu *, Shengqi Zhu, Jingwei Xu, Lan Lan, Ximin Li and Yiqun Zhang

National Key Laboratory of Radar Signal Processing, Xidian University, Xi'an 710071, China; sqzhu@xidian.edu.cn (S.Z.); jwxu@xidian.edu.cn (J.X.); lanlan@xidian.edu.cn (L.L.); xmli@xidian.edu.cn (X.L.); yiqzhang@stu.xidian.edu.cn (Y.Z.)

* Correspondence: zhixia@stu.xidian.edu.cn

Abstract: In the present complex electromagnetic environment, radar target detection is threatened by different kinds of interferences, especially mainlobe deceptive interference, which occupies the same energy distributions of targets spatially, meaning that targets and interferences cannot be discriminated. To make matters worse, the number of suppressible interferences is limited by the number of physical array elements, leading to the degradation of the suppression performance of traditional radar. In this work, we propose a frequency-increment-based interference suppression method for minimum redundancy frequency diverse array multiple-input multiple-output (MR-FDA-MIMO) radar, which effectively solves the aforementioned two problems. The interference suppression method consists of two steps: (i) in the sidelobe barrage interference suppression stage, the interference-plus-noise covariance matrix is reconstructed to overcome the influence of the true targets and mainlobe deceptive interference on the performance of the beamformer; (ii) in the mainlobe deceptive interference suppression stage, a nonadaptive beamforming method is employed to suppress mainlobe deceptive interference and overcome the impact of insufficient virtual samples on interference suppression performance. Additionally, we design a frequency-increment-based MR-FDA-MIMO radar, fully utilizing the advantages of the virtual array to enhance interference suppression performance and increase the number of interferences. Numerical experiments undertaken demonstrate the effectiveness of the algorithm under different scenarios.

Keywords: frequency diverse array; multiple-input multiple-output radar; minimum redundancy array; nonadaptive beamforming; frequency increment

check for updates

Citation: Wu, Z.; Zhu, S.; Xu, J.; Lan, L.; Li, X.; Zhang, Y. Frequency Increment Design Method of MR-FDA-MIMO Radar for Interference Suppression. *Remote Sens.* **2023**, *15*, 4070. https://doi.org/10.3390/rs15164070

Academic Editor: Dusan Gleich

Received: 25 May 2023
Revised: 13 August 2023
Accepted: 15 August 2023
Published: 17 August 2023

1. Introduction

The development of electronic countermeasures (ECM) technology has led to the existence of various types of interference, with the most significant being mainlobe deceptive interference. Mainlobe deceptive interference significantly diminishes the accuracy of true target detection and causes substantial distortion of the beam pattern [1,2]. False targets possess the same power and angle as the true target, resulting in common mainlobe deceptive interference that can easily confuse radar systems, making accurate identification of the true target difficult. Jammers intercept radar waveforms and generate false targets by modulating, delaying, and retransmitting them [3]. The presence of false targets poses significant threats to the detection and tracking of true targets, highlighting the urgent need for the development of deceptive interference suppression technology.

The field of electronic warfare has witnessed the emergence of numerous anti-interference technologies, such as adaptive beamforming and space-time adaptive processing (STAP). Among these, the minimum variance distortionless response (MVDR) method [4] is particularly effective for suppressing interference through beamforming. However, the focus of most of these methods is on suppressing sidelobe interference. Furthermore, various techniques have been proposed for the suppression of mainlobe interference [5–8]. These

techniques utilize the discrepancies between true targets and interference in various domains, including frequency, time, and polarization, in order to distinguish and suppress mainlobe interference. Furthermore, a method to counter mainlobe interference through proposed feature projection has been developed [8]. This technique utilizes the eigen-beams of interference to determine the extent of mainlobe interferences and implements robust countermeasures against multiple mainlobe interferences. In [9], a mainlobe interference suppression technique based on network radar was proposed. Similarly, a compound interference countermeasure technique based on networked radar was proposed; this technique operates at the physical layer of data [10]. A method based on robust blind source separation has been developed for mitigating mainlobe interference, taking into account the unknown number of interference sources [11]. However, despite the effectiveness of these techniques in mitigating mainlobe interference to some extent, the high fidelity of false targets remains a major limitation. Consequently, there is a need for radar systems with a greater number of degrees of freedom (DOFs).

Recent research has demonstrated that frequency diverse array (FDA) radar exhibits additional DOFs in the range domain [12–16]. Subsequent studies have integrated FDA with multiple-input multiple-output (MIMO) technology [17], facilitating the segregation of transmit signals in the receive dimension, thereby effectively acquiring range domain information and yielding additional DOFs [18–25]. FDA-MIMO radar exhibits degrees of freedom in the distance domain, offering advantages in both true target identification and false target suppression [26–31]. In this context, the initial focus concerns data-dependent beamforming, where a two-dimensional beamformer is designed specifically to mitigate the effects of false targets in the mainlobe [28]. Furthermore, a data-independent, two-dimensional beamformer has been specifically designed to improve robustness against errors by amplifying the depth and width of the nulls [29]. Moreover, a polarization-based technique has been developed in [30] for suppressing deceptive interference in polarized FDA-MIMO radar. This technique optimizes frequency increments to enhance both interference suppression performance and robustness. In addition, an optimization model for a coherent FDA radar-based transmit-receive two-dimensional beamformer has been developed [31]; this model demonstrates advantages in suppressing interference. While the aforementioned method offers significant advantages in suppressing false targets compared to traditional radar, the capacity to suppress false targets is constrained by the system's degrees of freedom, particularly by the number of transmit elements. In other words, the number of suppressed interferences cannot exceed the number of transmit elements. Consequently, in practical scenarios, an increase in the number of false targets necessitates a corresponding increase in the number of elements, leading to substantial resource consumption. Thus, addressing the challenge of surpassing the limitation on the number of elements to effectively suppress a larger number of false targets remains a significant problem.

In order to address the aforementioned issues, complex geometric arrays have been designed [32–35] which overcome the DOFs limitation of radar elements and involve addition of virtual DOFs. Initially, these specialized sparse arrays were utilized for parameter estimation purposes. In [35–40], a novel method for estimating angles is presented. In [38], a target parameter estimation method using two-dimensional sparse arrays is presented. Simulation results obtained demonstrate that a nested array with N elements is capable of estimating $O(N^2)$ parameters. A sparse array radar system that combines FDA-MIMO array radar and co-prime array has been developed. This system enhances localization accuracy for multiple targets [39,40]. Furthermore, in [41], an introduced algorithm for dimensionality reduction and robust space-time adaptive processing (STAP) is presented, which is based on sparse array radar. This algorithm utilizes the orthogonal matching pursuit algorithm to recover the clutter subspace and subsequently applies the STAP method for clutter suppression. Similarly, in [42], a channel selection strategy is proposed based on the angle-Doppler domain to address the dimensionality reduction problem of clutter rank in the STAP method. Furthermore, recognizing that the system's degrees of freedom

(DOFs) imposes limitations on suppression interference numbers, extensive research has been conducted on beamformers based on sparse arrays [43–45]. In [43], simulation results demonstrated that, when the number of elements was the same, beamformers based on minimum redundancy array (MRA) exceeded the interference suppression performance of uniform linear arrays (ULA) beamformers. In [44], a robust beamformer based on sparse arrays is proposed, overcoming the limitation whereby interference suppression is restricted by the number of physical units. Since general adaptive beamforming algorithms designed for ULA are unable to fully harness the characteristics offered by sparse arrays, a beamforming algorithm suitable for sparse co-prime arrays was introduced [45]. The previously mentioned beamforming methods mainly emphasize the suppression of sidelobe interference, while neglecting the suppression of false targets. To address this issue, in [46,47], a novel approach is proposed that combines FDA-MIMO radar with MRA and uses a data-independent beamforming method for MR-FDA-MIMO radar. In MR-FDA-MIMO radar, the number of suppressed mainlobe deceptive interferences exceeds the system DOFs, indicating that it suppresses more interferences than the number of physical transmit array elements. However, the current MR-FDA-MIMO model overlooks the design considerations for virtual arrays with frequency increments, resulting in underutilization of the extended virtual degrees of freedom. Therefore, to effectively suppress multiple mainlobe deceptive interferences, incorporating the design based on virtual arrays with frequency increments becomes essential.

This study presents a designed frequency increment scheme based on MR-FDA-MIMO radar to effectively utilize the available virtual DOFs and mitigate performance degradation resulting from the overlap of true and false targets in interference suppression. The proposed approach comprises two stages of beamforming—(a) a robust MVDR beamforming is employed in the receive domain to suppress sidelobe interference, and (b) a non-adaptive beamformer is utilized in the equivalent transmit domain to suppress multiple false targets—and design of a frequency increment based on the virtual array, effectively exploiting the virtual DOFs.

The innovate features of the proposed method are summarized as follows:

(i) In the context of mitigating multiple mainlobe deceptive interferences in MR-FDA-MIMO radar, a frequency increment based on a virtual array is developed, effectively leveraging the virtual degrees of freedom of MR-FDA-MIMO radar, resulting in improvements in both the number of suppressed interferences and interference performance.

(ii) In the interference suppression stage, various beamforming methods are employed. In the receive beamforming stage, because the sample covariance matrix includes both target and mainlobe deceptive interference information, the interference-plus-noise covariance matrix is reconstructed, and an MVDR beamformer is employed for sidelobe interference suppression. In the transmit beamforming stage, a nonadaptive beamformer is employed for mainlobe deceptive interference suppression, addressing the challenge of inadequate virtual samples.

In this work, Section 2 introduces the signal model with deceptive interference and barrage interference. In Section 3, a method for suppressing mainlobe and sidelobe interferences of the MR-FDA-MIMO radar is discussed, and the frequency increment redesigned based on virtual arrays is considered. The simulation and performance analysis results are presented in Section 4. Conclusions are drawn in Section 5.

2. MR-FDA-MIMO Radar Signal Model

Figure 1 shows the transmit array model of MR-FDA-MIMO radar, where the transmit array is a sparse MRA array composed of M elements, and the receive array is a ULA composed of N elements, with M and N being equal. Table 1 provides the MRA element configuration [32]. Figure 1 shows the 7-element MRA array. The 7-element MRA can estimate the correlation function of 0–17d spatial lags, covering the DOFs of 17d, where d is the inter-element spacing, which is usually taken as half the wavelength. However, the

7-element ULA can only estimate the correlation function of 0–6d spatial lags and can only cover the DOFs of 6d. The DOFs of MRA is obviously larger than that of ULA under the same array element.

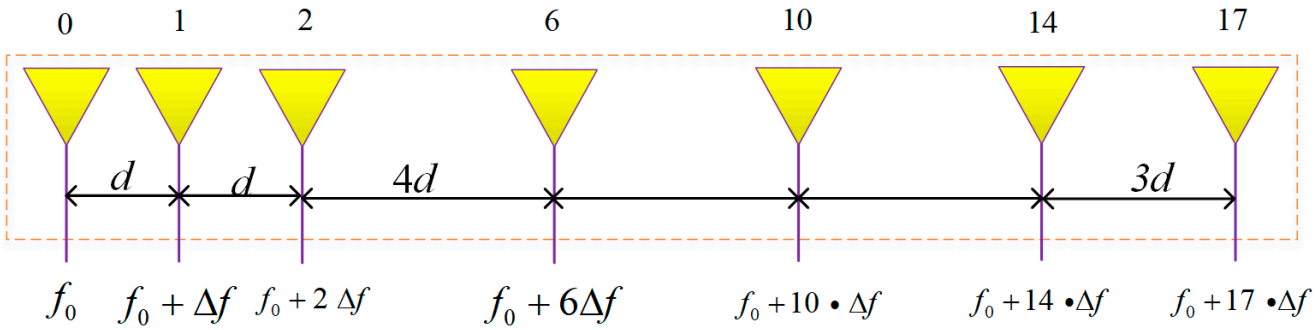

Figure 1. 7-element MRA.

Table 1. Configuration of the MRA selected from [32].

Number of Array Element	Array Element Locations
3	0 1 3
4	0 1 4 6
5	0 1 4 7 9
6	0 1 2 6 10 13
7	0 1 2 6 10 14 17
8	0 1 2 11 15 18 21 23

Without loss of generality, the frequency of the m-th transmit array element is

$$f_m = f_0 + \Delta f \mathbb{T}_m \; m = 1, 2, \ldots, M \tag{1}$$

where f_0 is the basic frequency, Δf is a small frequency increment, and $\mathbb{T}_m$ represents the position of the MRA element.

The transmit signal by the m-th element can be modeled as

$$s_m(t) = \sqrt{\frac{E}{M}} \varphi_m(t) e^{j2\pi f_m t}, 0 \le t \le T \tag{2}$$

where E is the transmit energy, T is the radar pulse duration, and $\varphi_m(t)$ is the baseband envelope, which is satisfied with the orthogonality condition.

Assuming a single point target at a far-field position (R_0, θ_0), the echo received by the n-th(n = 1, 2, . . ., N) receive array element can be denoted as:

$$\begin{aligned} y_n(t-\tau) &= \xi \sum_{m-1}^{M} s_m(t-\tau_{m,n}) \approx \xi \sum_{m-1}^{M} \varphi_m(t-\tau_0) e^{j2\pi f_m (t-\tau_{m,n})} \\ &= \xi e^{j2\pi f_0 (t-\tau_0)} e^{j2\pi \frac{d_R}{\lambda_0}(n-1)\sin(\theta_0)} \sum_{m-1}^{M} s_m(t-\tau_0) e^{j2\pi \Delta f T_m (t-\tau_0)} e^{j2\pi \frac{d}{\lambda_0} T_m \sin(\theta_0)} \end{aligned} \tag{3}$$

where ξ is the complex coefficient, $d_R = \lambda_0/2$ denotes the spacing between the receive elements, $\lambda_0 = c/f_0$ is the wavelength, and $\tau_{m,n} = \frac{2R_0 - d_R(n-1)\sin(\theta_0) - dT_m \sin(\theta_0)}{c}$ is the round-trip delay of the echo.

The receive echo processing flow of the MR-FDA-MIMO radar receiver is shown in Figure 2 [48,49]. Therefore, the snapshot received can be expressed in a simple form as [47–49]

$$\boldsymbol{x}_S = \beta_S \boldsymbol{b}(\theta_0) \otimes \boldsymbol{a}(R_0, \theta_0) \tag{4}$$

where $\beta_S = \xi e^{j2\pi\frac{2R_0}{\lambda_0}}$. $\boldsymbol{a}(R_0, \boldsymbol{\theta}_0) \in \mathbb{C}^{M\times 1}$ is the transmit steering vector composed of range and angle, which can be modeled as

$$\boldsymbol{a}(R_0, \boldsymbol{\theta}_0) = \left[1, e^{j2\pi\frac{d}{\lambda_0}\mathbb{T}_2 \sin(\boldsymbol{\theta}_0)} e^{-j2\pi\Delta f\frac{2R_0}{c}\mathbb{T}_2}, \ldots, e^{j2\pi\frac{d}{\lambda_0}\mathbb{T}_M \sin(\boldsymbol{\theta}_0)} e^{-j2\pi\Delta f\frac{2R_0}{c}\mathbb{T}_M}\right]^T \tag{5}$$

and $\boldsymbol{b}(\boldsymbol{\theta}_0) \in \mathbb{C}^{N\times 1}$ is the receive steering vector containing angle information, which can be modeled as

$$\mathbf{b}(\theta_0) = \left[1, e^{j2\pi\frac{d_R}{\lambda_0}\sin(\theta_0)}, \cdots, e^{j2\pi\frac{d_R}{\lambda_0}(N-1)\sin(\theta_0)}\right]^T \tag{6}$$

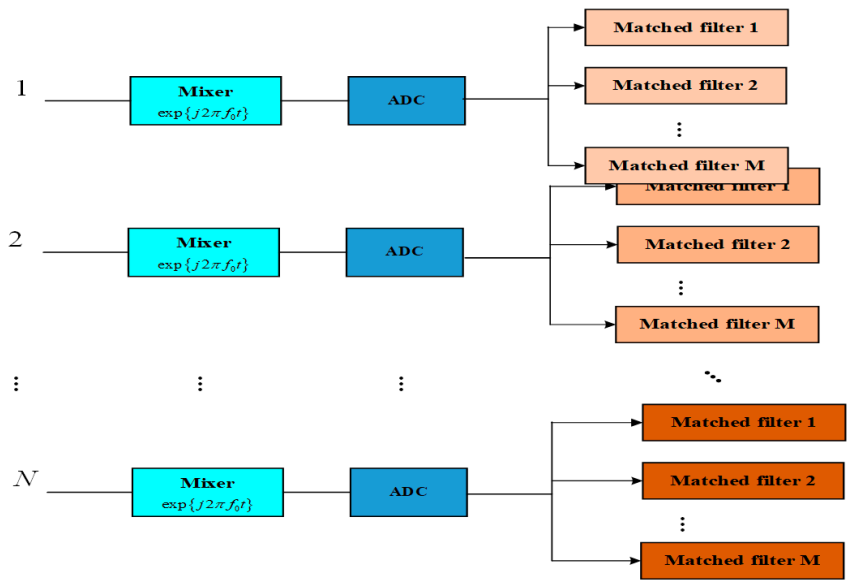

Figure 2. Signal processing at the receiver.

Assuming there are $\mathbb{F}$ false targets, the angle of each false target is θ_j, and the range is R_f. Due to the different time delays of the false targets, the R_f values of each false target are different [28,50]. The false targets lag behind the true target by at least one maximum unambiguous range (Figure 3) [28,50,51]. After matching filtering (Figure 2), the echo form of the f-th false target is

$$\boldsymbol{x}_f = \beta_f \boldsymbol{b}(\theta_j) \otimes \boldsymbol{a}\left(R_f, \theta_j\right) \tag{7}$$

where β_f denotes the complex coefficient of the f-th (f = 1, 2, …, $\mathbb{F}$) false target, and $R_f = R_j + \frac{c\tau_f}{2}$, τ_f indicates the time delay.

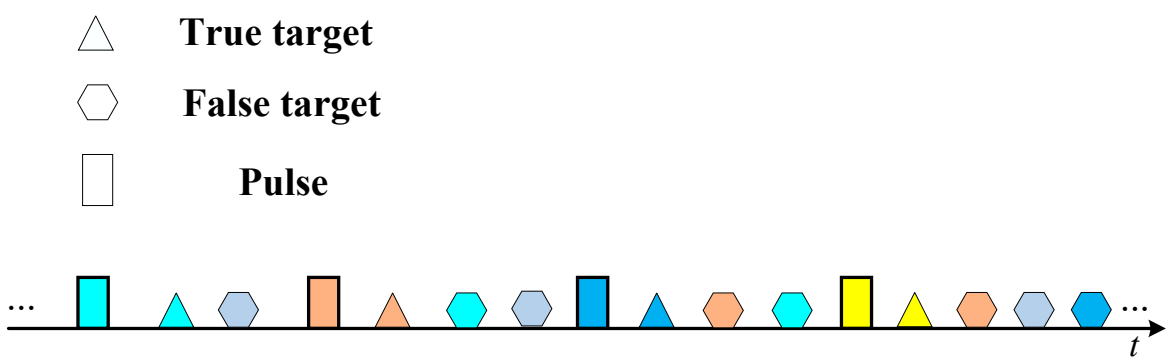

Figure 3. Distribution of false targets.

$\boldsymbol{a}\left(R_f, \boldsymbol{\theta}_j\right) \in \mathbb{C}^{M\times 1}$ and $\boldsymbol{b}\left(\boldsymbol{\theta}_j\right) \in \mathbb{C}^{N\times 1}$ are the transmit and receive steering vectors, respectively, which are given as

$$\boldsymbol{a}\left(R_f, \boldsymbol{\theta}_j\right) = \left[1, e^{j2\pi\frac{d}{\lambda_0}\mathbb{T}_2 \sin(\boldsymbol{\theta}_j)} e^{-j2\pi\Delta f\frac{2R_f}{c}\mathbb{T}_2}, \ldots, e^{j2\pi\frac{d}{\lambda_0}\mathbb{T}_M \sin(\boldsymbol{\theta}_j)} e^{-j2\pi\Delta f\frac{2R_f}{c}\mathbb{T}_M}\right]^T \tag{8}$$

$$\mathbf{b}\left(\theta_j\right) = \left[1, e^{j2\pi\frac{d_R}{\lambda_0}\sin(\theta_j)}, \cdots, e^{j2\pi\frac{d_R}{\lambda_0}(N-1)\sin(\theta_j)}\right]^T \tag{9}$$

The sidelobe barrage interference model is [52]

$$\boldsymbol{x}_{\mathrm{J}} = \sum_{k=1}^{K} \beta_k \boldsymbol{b}(\theta_k) \otimes \boldsymbol{n}_{\mathrm{T}} \tag{10}$$

where β_k is a zero-mean complex Gaussian random variable, $\boldsymbol{n}_{\mathrm{T}} \in \mathbb{C}^{M\times 1}$ is the noise-like transmit steering vector of the barrage interference, and $\boldsymbol{n}_{\mathrm{T}} \sim CN(0, \boldsymbol{I}_M)$. $\boldsymbol{b}(\theta_k) = \left[1, e^{j2\pi\frac{d_R}{\lambda_0}\sin(\theta_k)}, \cdots, e^{j2\pi\frac{d_R}{\lambda_0}(N-1)\sin(\theta_k)}\right]^T \in \mathbb{C}^{N\times 1}$ is the receive steering vector of the barrage interference containing the angle information.

The output signal is represented as [21,47].

$$\boldsymbol{x} = \boldsymbol{x}_{\mathrm{s}} + \sum_{f=1}^{F} \boldsymbol{x}_f + \boldsymbol{x}_{\mathrm{J}} + \boldsymbol{x}_n \tag{11}$$

where $\boldsymbol{x}_n$ is assumed to be white Gaussian noise, σ_n^2 is the noise variance, and $\boldsymbol{I}_{MN}$ denotes an $MN \times MN$ identity matrix.

Notice that we are considering mainlobe deceptive interference, also known as the false target, so $\boldsymbol{\theta}_j = \boldsymbol{\theta}_0$.

3. Based on the MR-FDA-MIMO Radar Interference Suppression Method

In this section, in order to take advantage of the transmit dimension virtual DOFs of the MR-FDA-MIMO radar, the false target and sidelobe interference are suppressed, respectively [46,47]. Firstly, the robust MVDR is used to suppress sidelobe interference in the receive port; secondly, a difference co-array is used to process equivalent transmit dimension data to obtain long virtual array data, and a nonadaptive method is used to suppress the false target. Considering that the virtual DOFs is fully used to suppress multiple false targets, the Δf based on a long virtual array is redesigned; compared with the Δf based on a physical array, the number of false targets suppressed is increased.

3.1. Sidelobe Barrage Interference Suppression

The received dimension data are

$$\begin{aligned} \boldsymbol{X} &= \mathrm{res}(\boldsymbol{x}) \in \mathbb{C}^{M\times N} \\ \overline{\boldsymbol{X}} &= \mathrm{mat}(\boldsymbol{X}) \in \mathbb{C}^{N\times 1} \end{aligned} \tag{12}$$

where $\mathrm{res}(\cdot)$ and $\mathrm{mat}(\cdot)$ represent the reconstruction operators. The transformation of the multi-dimensional dataset is illustrated Figure 4. The data $\boldsymbol{x}$ is transformed into a dimension of $NM*L$ after undergoing matched filtering. Subsequently, the data undergoes the $\mathrm{res}(\cdot)$ reconstruction operation, resulting in a dimension of $N*M*L$ (Figure 4a). To obtain the receive dimensional data, further $\mathrm{mat}(\cdot)$ reconstruction operation is conducted, leading to a dimension of $N*L$ for the data (Figure 4b). Applying sidelobe interference suppression processing on the receive dimensions allows for obtaining the transmit dimensional data, with a data dimension of $M*L$ (Figure 4c).

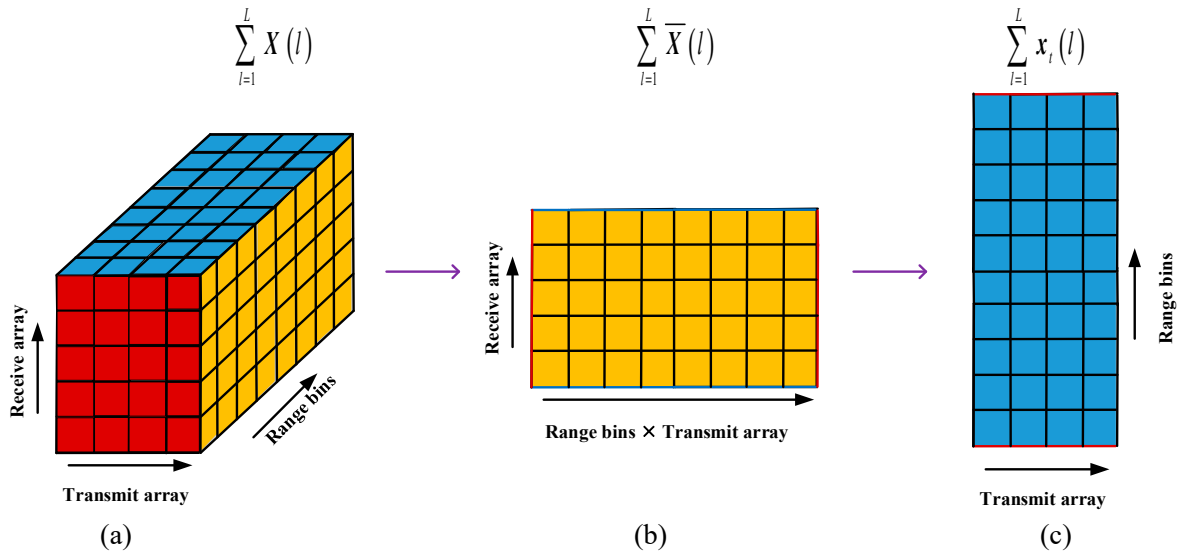

Figure 4. Data cube changes.

The covariance matrix is

$$\boldsymbol{R} = \frac{1}{L}\sum\nolimits_{l=1}^{L} \overline{\mathbf{X}}(l)\overline{\mathbf{X}}^{H}(l) \tag{13}$$

where L is the number of snapshots, and $\overline{\mathbf{X}}(l)$ is the l-th receive sample.

The obtained $\mathbf{R}$ includes not only sidelobe interference and noise, but also the targets. Therefore, the covariance matrix is reconstructed to obtain robust MVDR weights [53].

First, the Capone spatial spectrum estimator is used [53].

$$P(\boldsymbol{\theta}) = \frac{1}{\mathbf{b}^{H}(\boldsymbol{\theta})\mathbf{R}^{-1}\mathbf{b}(\boldsymbol{\theta})} \tag{14}$$

The covariance matrix is [53]

$$\overline{\mathbf{R}}_{j+n} = \int_{\Theta} P(\boldsymbol{\theta})\mathbf{b}(\boldsymbol{\theta})\mathbf{b}^{H}(\boldsymbol{\theta})d\boldsymbol{\theta} = \int_{\Theta} \frac{\mathbf{b}(\boldsymbol{\theta})\mathbf{b}^{H}(\boldsymbol{\theta})}{\mathbf{b}^{H}(\boldsymbol{\theta})\mathbf{R}^{-1}\mathbf{b}(\boldsymbol{\theta})}d\boldsymbol{\theta} \tag{15}$$

Where $\mathbf{b}(\boldsymbol{\theta})$ refers to the steering vector of the sidelobe barrage interference, and Θ represents the angles of the potential sidelobe barrage interferences other than the target.

The robust receive MVDR beamforming weight is [4]

$$\mathbf{w}_{\mathrm{Rec}} = \frac{\overline{\mathbf{R}}_{j+n}^{-1}\mathbf{b}(\boldsymbol{\theta}_0)}{\mathbf{b}(\boldsymbol{\theta}_0)^{H}\overline{\mathbf{R}}_{j+n}^{-1}\mathbf{b}(\boldsymbol{\theta}_0)} \tag{16}$$

The suppression of sidelobe interference can be expressed as

$$\begin{aligned} \boldsymbol{x}_t &= (\boldsymbol{w}_{\mathrm{Rec}} \otimes \boldsymbol{I}_M)^{H} \cdot \boldsymbol{x} \\ &= \boldsymbol{\beta}_s \boldsymbol{a}(R_0, \boldsymbol{\theta}_0) + \sum_{f=1}^{\mathbb{F}} \boldsymbol{\beta}_f \boldsymbol{a}\left(R_f, \boldsymbol{\theta}_0\right) + (\boldsymbol{w}_{\mathrm{Rec}} \otimes \boldsymbol{I}_M)^{H} \cdot \boldsymbol{x}_n \end{aligned} \tag{17}$$

3.2. Mainlobe Deceptive Interference Suppression

The false target suppression is divided into three steps: (i) expanding the virtual transmit DOFs; (ii) using a nonadaptive beamforming method to suppress false targets; (iii) designing appropriate frequency increments to make full use of the virtual DOFs.

3.2.1. Range Compensation

The transmit frequency of the targets is range-dependent, and this range dependence can be compensated [48]. The compensated data are

$$\widetilde{\boldsymbol{x}} = \beta_s \cdot \boldsymbol{a}(\theta_0) + \sum_{f=1}^{\mathbb{F}} \beta_f \boldsymbol{a}(p, \theta_0) + \boldsymbol{x}_n \tag{18}$$

where p is the number of false target ambiguities. It is assumed that the true target has zero range ambiguity.

The transmit frequency of the targets is

$$\widetilde{f}_{\mathrm{Ts}} = \frac{d}{\lambda_0} \sin\theta_0 \tag{19}$$

$$\widetilde{f}_{\mathrm{T}f} = \frac{d}{\lambda_0} \sin\theta_0 - \frac{2\Delta f}{c} p R_u \tag{20}$$

where $R_u = c/(2f_r)$ is the maximum unambiguous range, and f_r is the pulse repetition frequency(PRF). Δf can be represented as [51,54]

$$\Delta f = f_r \left(z + \frac{i}{pM} \right), i = 1, 2, \ldots, M-1 \tag{21}$$

where z represents an integer value, which is typically considered negligible, and p denotes the number of delayed pulses associated with the false target.

Substituting Equation (21) into Equation (20), it can be concluded that, when the delay pulse of the false target is p, the transmit frequency of the false target corresponds to the frequency of the p-th null of the beampattern. When the delay pulse of the false target ranges from 1 to $(M-1)$, it corresponds to the 1 to $(M-1)$-th nulls of the beampattern, and, thus, can effectively suppress the 1 to $(M-1)$-th false targets in Figure 5.

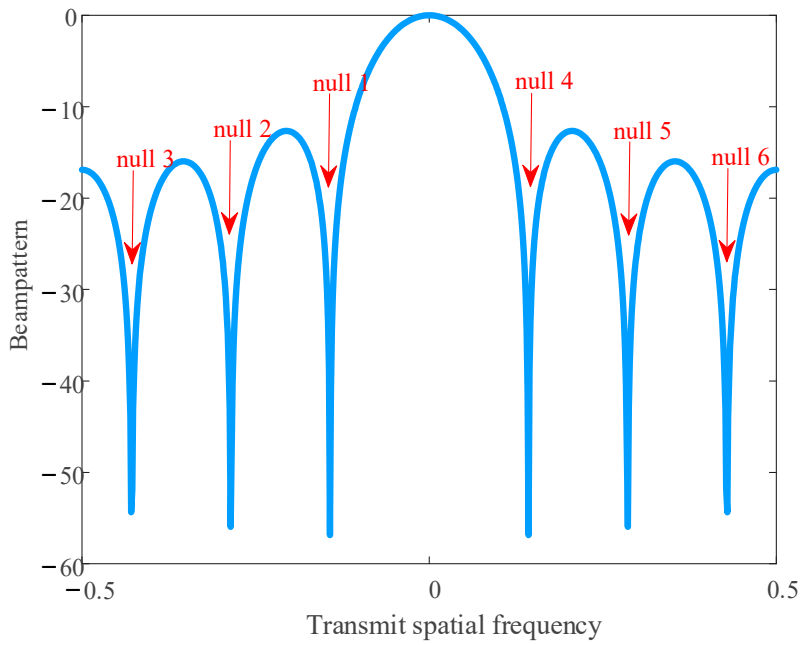

Figure 5. Beampattern with 7−element ULA.

3.2.2. Virtual DOFs Expansion

Performing difference co-array processing on the equivalent transmit dimension data

$$\boldsymbol{R}_t = \left(\frac{1}{L}\sum_{l=1}^{L}\widetilde{\boldsymbol{x}}(l)\widetilde{\boldsymbol{x}}^{\mathrm{H}}(l)\right) = \sum_{q=1}^{Q}\sigma_q^2\boldsymbol{a}_q\boldsymbol{a}_q^H + \sigma_n^2\boldsymbol{I}_M \tag{22}$$

where Q is the number of targets.

The long virtual array data can be obtained by vectorizing the difference co-array data. Therefore, the virtual array signal is

$$\boldsymbol{r} = \mathrm{vec}(\boldsymbol{R}_t) = \boldsymbol{B}\boldsymbol{h} + \sigma_n^2\boldsymbol{i} \tag{23}$$

where $\boldsymbol{B} = \left[\boldsymbol{b}(\theta_1), \boldsymbol{b}(\theta_2), \cdots, \boldsymbol{b}(\theta_Q)\right] \in \mathbb{C}^{M^2\times Q}$ is the steering vector matrix, $\boldsymbol{b}(\boldsymbol{\theta}_q) = \boldsymbol{a}\left(\widetilde{f}_{\mathrm{T}}^q\right) \otimes \boldsymbol{a}^*\left(\widetilde{f}_{\mathrm{T}}^q\right)$ is the virtual steering vector, $\boldsymbol{h} = \left[\sigma_1^2, \sigma_2^2, \cdots, \sigma_Q^2\right]^T \in \Re^{Q\times 1}$ contains the power of K targets, and $\boldsymbol{i} = \mathrm{vec}(\boldsymbol{I}_M)$.

The vector z contains duplicate elements and is in disorder. Therefore, matrix G is used to sort z in order and to remove duplicate elements [45]. The de-redundant re-arrangement of $\boldsymbol{r}_{\mathrm{v}}$ can be written as

$$\boldsymbol{r}_{\mathrm{v}} = \boldsymbol{G}\boldsymbol{r} = \boldsymbol{B}_{\mathrm{v}}\boldsymbol{h} + \sigma_n^2\boldsymbol{i}_{\mathrm{v}} \tag{24}$$

where $G \in \{0,1\}^{M^2\times(2\mathbb{T}_M+1)}$, and $\boldsymbol{B}_{\mathrm{v}} = \left[\boldsymbol{b}_{\mathrm{v}}(\theta_1), \boldsymbol{b}_{\mathrm{v}}(\theta_2), \cdots, \boldsymbol{b}_{\mathrm{v}}(\theta_Q)\right]$ is the steering matrix of the virtual ULA, where $\mathbb{V} = \mathbb{T}_M$. $\boldsymbol{b}_{\mathrm{v}}(\boldsymbol{\theta}_q) = \exp\left\{j2\pi\widetilde{f}_{\mathrm{T}}^q D_{\mathrm{v}}{}^{\mathrm{T}}\right\}$ is the virtual ULA steering vector, and $D_{\mathrm{v}} = \{-\mathbb{V}d, (-\mathbb{V}+1)d, \cdots, 0, \cdots, (\mathbb{V}-1)d, \mathbb{V}d\}$ represents the element position of the virtual ULA. $\boldsymbol{i}_{\mathrm{v}} = [0, \cdots, 0, 1, 0, \cdots, 0]^T \in \mathbb{R}^{D_{\mathrm{v}}\times 1}$ is a real-valued column vector with a central position of one, with all other positions being zero.

Figure 6 illustrates the distribution of element locations for a 7-element MRA and a virtual ULA. As illustrated, the physical elements form a sparse array, and a virtual ULA with a greater number of elements than the physical array is obtained through difference co-array processing.

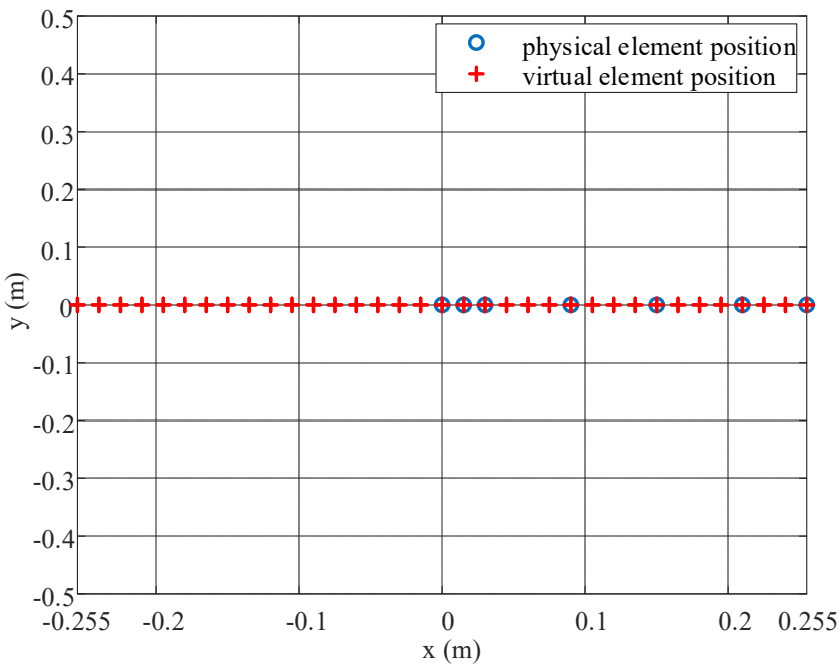

Figure 6. Element position.

3.2.3. Mainlobe Deceptive Interference Suppression

Figure 7 shows the positions of the targets in the transmit beampattern at different numbers of array elements when $\Delta f = f_r\left(z + \frac{i}{pM}\right)$ is used. From Figure 7a, it can be seen that, when p = 4, for the case of M array elements, the false target with 4 delay pulses coincides precisely with the 4-th null of the beampattern. However, for the case of $2\mathbb{V}+1$ array elements, the false target with 4 delay pulses does not coincide with the 4-th null of the beampattern. When p = M, as shown in Figure 7b, the false target coincides with the true target in the mainlobe of the beampattern regardless of whether the array has M or $2\mathbb{V}+1$ elements. This is because the frequency increment in Equation (21) is designed based on the physical array. When the delay pulse numbers of the false targets are an integer multiple of M, the true and false targets coincide.

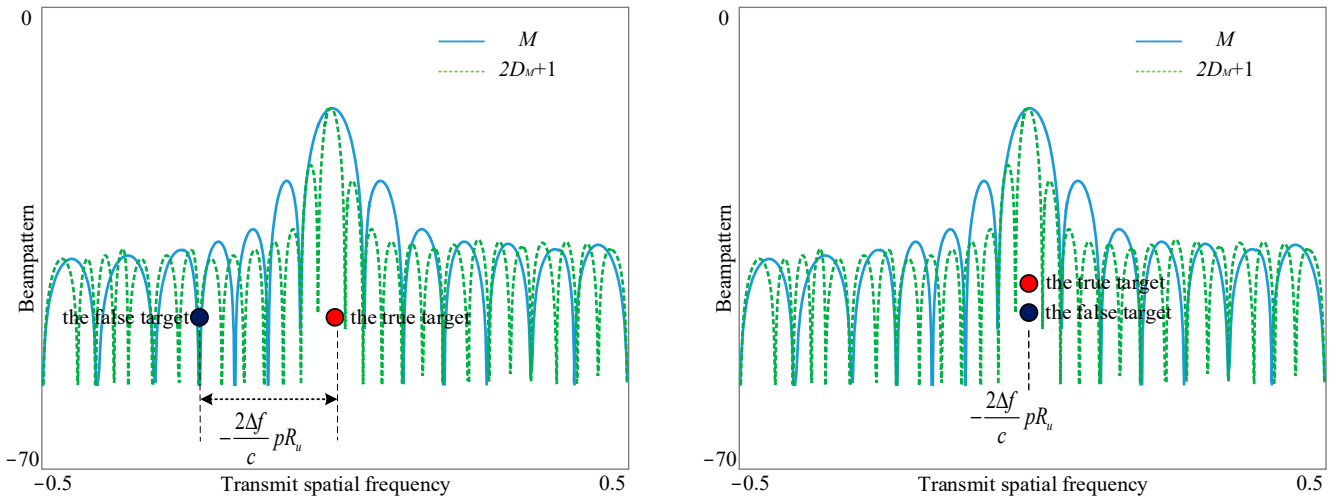

Figure 7. Distribution of true and false targets in the transmit beampattern. (**a**) p = 4. (**b**) p = M.

(i) Based on virtual ULA design Δf

To fully utilize the virtual DOFs to suppress multiple false targets, it is necessary to redesign Δf based on a virtual array. The transmit steering vectors are summed to obtain an equivalent normalized transmit beampattern, which is

$$\begin{aligned} P\left(\widetilde{f}_{\mathrm{T}}\right) &= \boldsymbol{w}_{\mathrm{T}}^{\mathrm{H}}\widetilde{\boldsymbol{a}}\left(\widetilde{f}_{\mathrm{T}}\right) = \tfrac{1}{2\mathbb{V}+1}\cdot\sum_{m=-\mathbb{V}}^{\mathbb{V}} e^{j2\pi m\widetilde{f}_{\mathrm{T}}} \\ &= \tfrac{1}{2\mathbb{V}+1}\cdot\frac{e^{j2\pi(-\mathbb{V})\widetilde{f}_{\mathrm{T}}}-e^{j2\pi(\mathbb{V}+1)\widetilde{f}_{\mathrm{T}}}}{1-e^{j2\pi\widetilde{f}_{\mathrm{T}}}} = \tfrac{1}{2V+1}\cdot\frac{e^{j2\pi(-\mathbb{V})\widetilde{f}_{\mathrm{T}}}\left(1-e^{j2\pi(2\mathbb{V}+1)\widetilde{f}_{\mathrm{T}}}\right)}{1-e^{j2\pi\widetilde{f}_{\mathrm{T}}}} \\ &= \tfrac{1}{2\mathbb{V}+1}\cdot\frac{e^{j\pi\widetilde{f}_{\mathrm{T}}}\left(e^{-j\pi(2\mathbb{V}+1)\widetilde{f}_{\mathrm{T}}}-e^{j\pi(2\mathbb{V}+1)\widetilde{f}_{\mathrm{T}}}\right)}{e^{j\pi\widetilde{f}_{\mathrm{T}}}\left(e^{-j\pi\widetilde{f}_{\mathrm{T}}}-e^{j\pi\widetilde{f}_{\mathrm{T}}}\right)} = \tfrac{1}{2\mathbb{V}+1}\cdot e^{j\pi\widetilde{f}_{\mathrm{T}}}\frac{\sin\left(\pi(2\mathbb{V}+1)\widetilde{f}_{\mathrm{T}}\right)}{\sin\left(\pi\widetilde{f}_{\mathrm{T}}\right)} \end{aligned} \tag{25}$$

where $\boldsymbol{w}_{\mathrm{T}} = \frac{1}{2\mathbb{V}+1}[1,\ldots,1]^{\mathrm{T}} \in \mathbb{R}^{2\mathbb{V}+1}$, $\boldsymbol{a}_V\left(\widetilde{f}_{\mathrm{T}}\right) = [e^{-j2\pi\mathbb{V}\widetilde{f}_{\mathrm{T}}}, e^{-j2\pi(\mathbb{V}-1)\widetilde{f}_{\mathrm{T}}},\ldots,e^{j2\pi(\mathbb{V}-1)\widetilde{f}_{\mathrm{T}}}, e^{j2\pi\mathbb{V}\widetilde{f}_{\mathrm{T}}}] \in \mathbb{C}^{2\mathbb{V}+1}$ denotes the true target virtual transmit steering vector.

When the beampattern has a zero, the numerator of $P\left(\widetilde{f}_{\mathrm{T}}\right)$ becomes zero, that is, $(2\mathbb{V}+1)\pi\widetilde{f}_{\mathrm{T}} = k\pi, k \in \mathbb{Z}^{+}$, while the denominator remains non-zero, that is $\pi\widetilde{f}_{\mathrm{T}} \neq k\pi, k \in \mathbb{Z}^{+}$. This will result in

$$\widetilde{f}_{\mathrm{T}} = \frac{k}{2\mathbb{V}+1} \tag{26}$$

For the first null with frequency $\widetilde{f}_{\mathrm{T}} = \frac{1}{2\mathbb{V}+1}$, if $u = \frac{1}{2\mathbb{V}+1}$, the false target with one delayed pulse will fall precisely on the first null. Therefore, the Δf for the false target with one delayed pulse is

$$\Delta f = f_r\left(z + \frac{1}{2\mathbb{V}+1}\right) \tag{27}$$

Therefore, when the false target has a delay of p pulses, the Δf is equal to

$$\Delta f = f_r\left(z + \frac{i}{p(2\mathbb{V}+1)}\right), i \in D_{\mathbb{V}} \tag{28}$$

(ii) Nonadaptive beamforming

The virtual ULA covariance matrix is $\boldsymbol{R}_{\mathrm{v}} = \boldsymbol{r}_{\mathrm{v}} * \boldsymbol{r}_{\mathrm{v}}^{\mathrm{H}}$, and it can be observed that, when $\boldsymbol{r}_{\mathrm{v}}$ is a single snapshot, the rank of the $\boldsymbol{R}_{\mathrm{v}}$ is deficient. In [55], a spatial smoothing method is proposed to increase the number of samples, but it suffers from the drawback of losing virtual DOFs. Therefore, a nonadaptive beamforming anti-interference method based on virtual ULA is designed. It should be noted that this nonadaptive method does not require samples during beamforming.

The nonadaptive weight vector is

$$\boldsymbol{w} = \boldsymbol{G}\cdot\mathrm{vec}\left[\boldsymbol{a}\left(\widetilde{f}_{\mathrm{Ts}}\right) \otimes \boldsymbol{a}^*\left(\widetilde{f}_{\mathrm{Ts}}\right)\right] = \left[e^{-j2\pi\widetilde{f}_{\mathrm{Ts}}\mathbb{V}}, \cdots, 1, \cdots, e^{j2\pi\widetilde{f}_{\mathrm{Ts}}\mathbb{V}}\right] \tag{29}$$

The final output is

$$y = \boldsymbol{w}^H \boldsymbol{r}_{\mathrm{v}} \tag{30}$$

4. Results

This section provides numerical examples to demonstrate the effectiveness of the proposed method. $\Theta \in ([-90°, -5°] \cup [5°, 90°])$. Note that, unless otherwise specified, Δf is set according to Equation (21).

It is assumed that the two false targets have delay pulse numbers of 1 and 3, respectively. The parameters are shown in Table 2.

Table 2. Simulation Parameters.

Parameter	Value	Parameter	Value
Transmit element number	7	Receive element number	7
Sample frequency	5 MHz	Reference frequency	10 GHz
Pulse repetition frequency (PRF)	5 KHz	Wavelength	0.03 m
Angle of the true target	0°	SNR	20 dB
Angle of the false target 1	0°	INR1	20 dB
Angle of the false target 2	0°	INR2	20 dB
Angle of the sidelobe interference 1	30°	INRn1	40 dB
Angle of the sidelobe interference 2	−30°	INRn2	40 dB

The power spectra of the targets as well as the sidelobe interference in MR-FDA-MIMO radar are shown in Figure 8. In Figure 8a, it can be observed that the true and false targets have equal height due to their equal power levels. However, the power of the sidelobe barrage interference is notably higher, resulting in a significantly elevated sidelobe interference level compared to the targets. Figure 8b demonstrates the ability to distinguish between the interference and the targets at the receive port, as well as between the true and false targets at the transmit port.

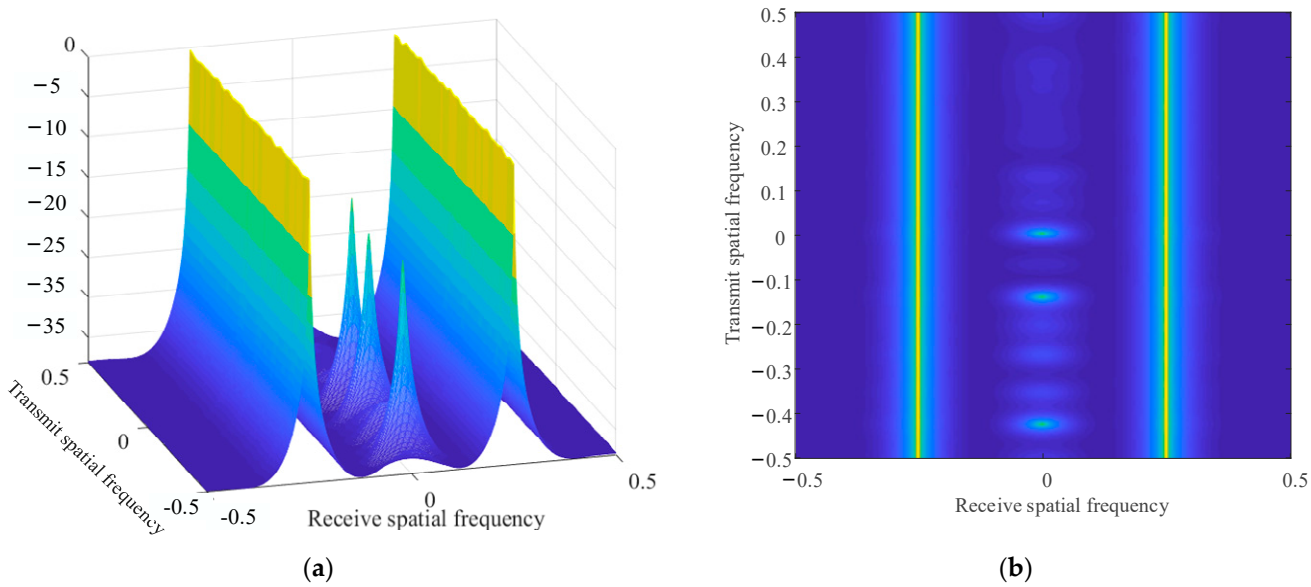

(**a**) (**b**)

Figure 8. Target and interference power spectrum. (**a**) Transmit-receive 2-D power spectrum. (**b**) 3-D power spectrum.

4.1. Sidelobe Barrage Interference Suppression

The beamforming results of various methods are presented in Figure 9, demonstrating that both MVDR beamforming and the sample matrix inversion (SMI) [56] method exhibit nulls in the sidelobe interference region. As depicted in the figure, the mainlobe of the SMI beampattern experiences distortion and deformation attributed to the target components present in the training data. In contrast, the robust MVDR beampattern preserves a robust and well-defined shape.

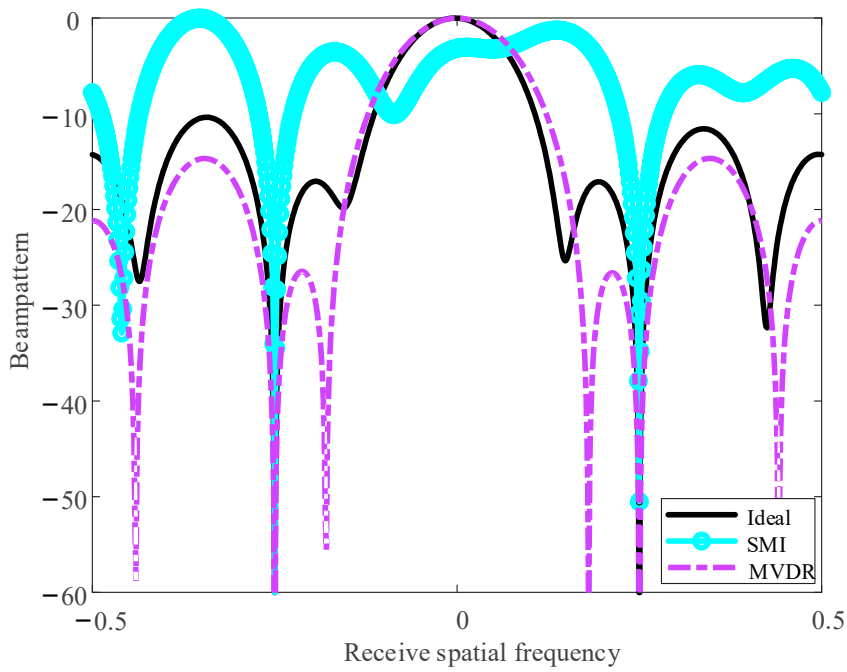

Figure 9. Normalized beampattern of receive port.

4.2. Mainlobe Deceptive Interference Suppression

This subsection analyzes scenarios that involve two or multiple false targets. The simulation is utilized to evaluate the impact of selecting Δf on the effectiveness of the false target.

The zones of mainlobe deceptive interference suppression are illustrated in Figure 10. The y-axis represents the number of delayed pulses for the false target, and the x-axis represents $u \times M$ ($u \times (2\mathbb{V}+1)$). Additionally, the color indicates the target power and the effectiveness of the interference suppression. Yellow indicates high true target output power, while blue denotes ineffective suppression of the false target. It is important to note that the complete suppression of false targets becomes challenging when the number of false targets exceeds the number of physical array elements. This is evident in Figure 10a where it is observed that the effectiveness of the interference suppression is compromised. As can be seen in Figure 10b, an increase in the number of virtual array elements results in enhanced interference suppression. Notably, in line with theoretical considerations, false targets with $1 \sim 2 \times \mathbb{V}$ delayed pulses are effectively suppressed when $u(2 \times \mathbb{V}+1)$, as they align with $1 \sim 2 \times \mathbb{V}$ nulls present in the beampattern. Furthermore, when $u(2 \times \mathbb{V}+1) = 0$ or $u(2 \times \mathbb{V}+1) = 1$, the false target aligns with the true target and becomes indistinguishable, thus leading to an inability to suppress the false target.

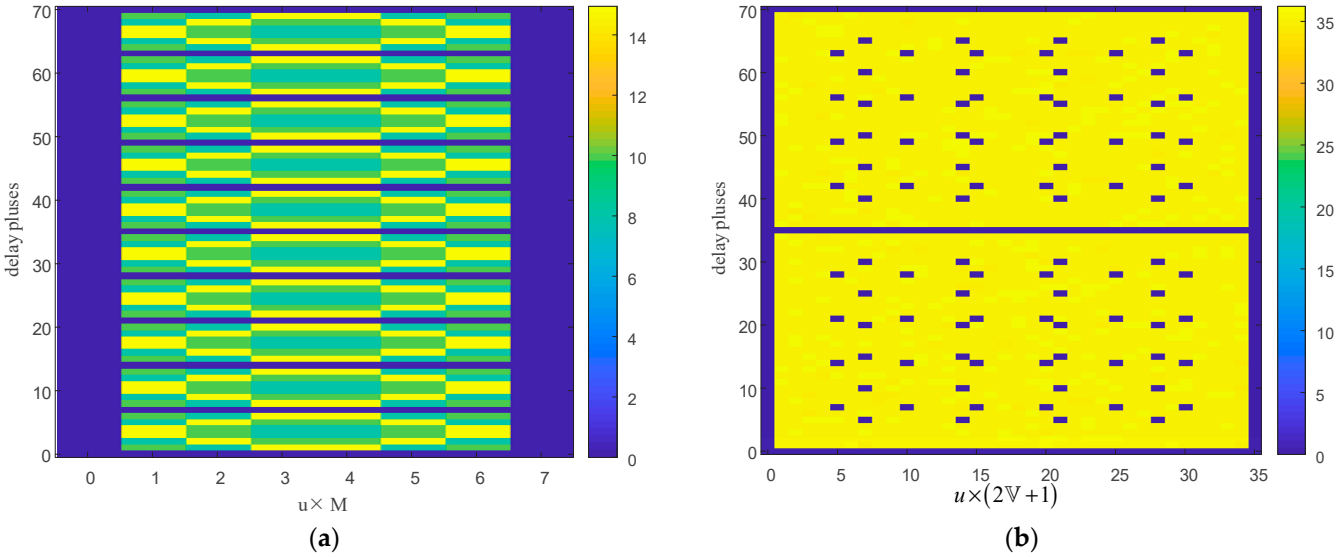

Figure 10. Suppression zone of false targets. (**a**) $\Delta f = f_r\left(z + \frac{i}{pM}\right)$. (**b**) $\Delta f = f_r\left(z + \frac{i}{p(2\mathbb{V}+1)}\right)$.

4.2.1. Two Mainlobe Deceptive Interferences Suppression

Different Δf values corresponding to the beampatterns are shown in Figure 11. The original 7-element MVDR method is a beamformer that utilizes physical array elements. The virtual array nonadaptive method is a beamformer that utilizes a virtual array. As shown in Figure 11a, for the frequency increment defined by Equation (21), false targets with p (p = 1, 3) delay pulses are situated within the p-th null of the original 7-element MVDR beampattern. However, in the nonadaptive method utilizing the virtual array beampattern, the false targets with p delay pulses do not align with the p-th null, resulting in underutilization of the DOFs provided by the virtual array. Conversely, when employing the frequency increment designated by Equation (28), the false targets with p delay pulses align with the p-th null in the beampattern shown in Figure 11b.

The output SINR results under different Δf values are shown in Figure 12. The performance of the original 7-element MVDR method deteriorates at high SNR due to the presence of the true targets in the samples. In contrast, the performance of the virtual array nonadaptive method remains constant and approaches the ideal performance curve. Upon careful examination of Figure 12a,b, it is evident that the original 7-element MVDR method approximates the ideal performance curve at low SNR when $\Delta f = f_r\left(z + \frac{i}{pM}\right)$. However, when $\Delta f = f_r\left(z + \frac{i}{p(2\mathbb{V}+1)}\right)$, the original 7-element MVDR method exhibits a decline in performance. By analyzing the beampattern in Figure 11b, it is observed, when

$\Delta f = f_r\left(z + \frac{i}{p(2\mathbb{V}+1)}\right)$ and $p = \{1, 3\}$, that the first null is in close proximity to the mainlobe, resulting in shifting.

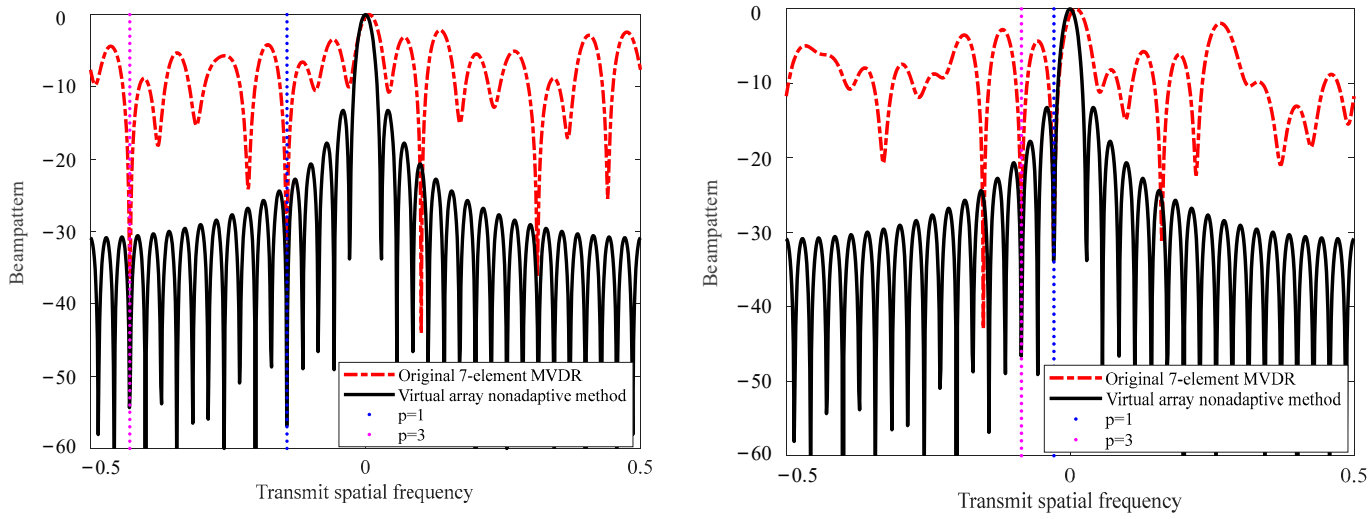

(**a**) (**b**)

Figure 11. Beampattern with different Δf. (**a**) $\Delta f = f_r\left(z + \frac{i}{pM}\right)$. (**b**) $\Delta f = f_r\left(z + \frac{i}{p(2\mathbb{V}+1)}\right)$.

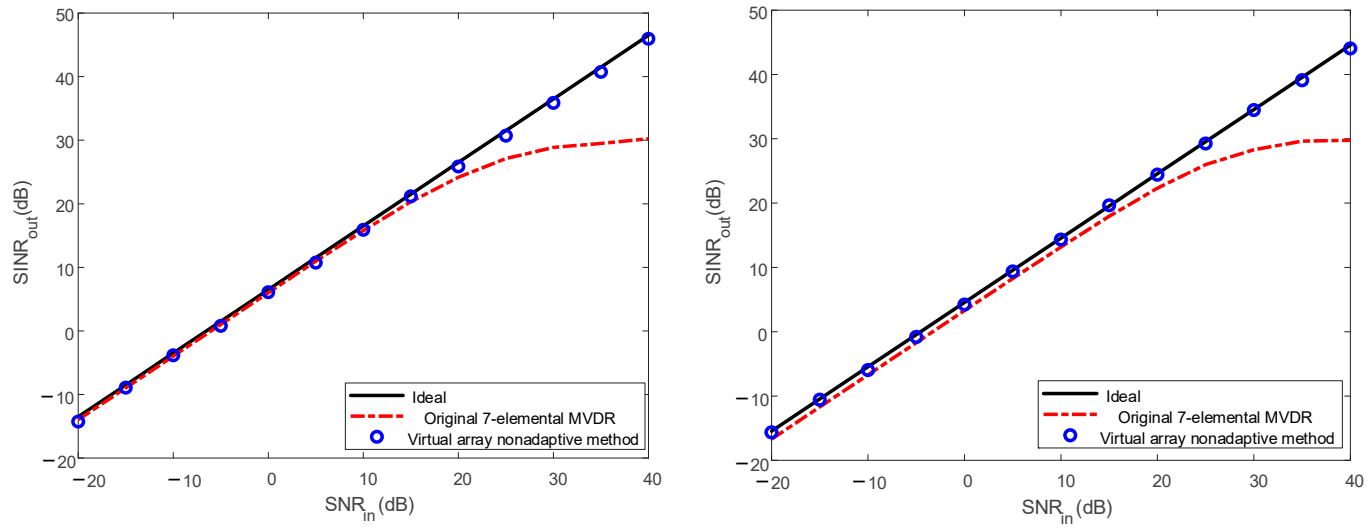

(**a**) (**b**)

Figure 12. Output SINR versus input SNR. (**a**) $\Delta f = f_r\left(z + \frac{i}{pM}\right)$. (**b**) $\Delta f = f_r\left(z + \frac{i}{p(2\mathbb{V}+1)}\right)$.

4.2.2. Multiple Mainlobe Deceptive Interferences Suppression

Subsequently, the influence of varying Δf values on the performance of interference suppression in the presence of multiple false targets was examined.

The beampattern of multiple false targets is shown in Figure 13. As illustrated by Figure 13a, in the case of $\Delta f = f_r\left(z + \frac{i}{pM}\right)$ and 14 false targets, the remaining false targets overlap with each other, with some located inside the mainlobe, resulting in significant distortion of the beampattern. Conversely, in the case of $\Delta f = f_r\left(z + \frac{i}{p(2\mathbb{V}+1)}\right)$, as depicted in Figure 13b, a narrow and undistorted mainlobe is observed, improving the resolution. Furthermore, all 14 false targets are visible in the power spectrum without overlapping the true target. Each false target precisely aligns with its respective null in the beampattern.

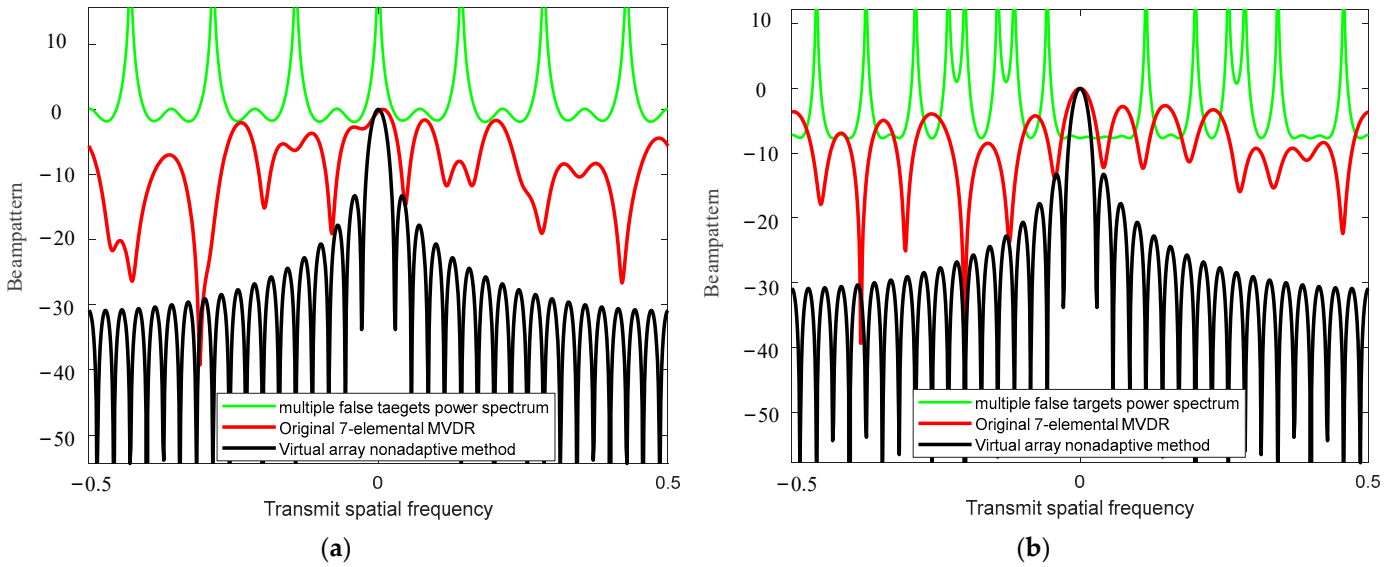

(**a**) (**b**)

Figure 13. Beampattern with 14 false targets. (**a**) $\Delta f = f_r\left(z + \frac{i}{pM}\right)$. (**b**) $\Delta f = f_r\left(z + \frac{i}{p(2\mathbb{V}+1)}\right)$.

The performance of multi-interference suppression in the MR-FDA-MIMO radar under different Δf values is analyzed in Figure 14. Based on Figure 14a, it can be concluded that neither the virtual array nonadaptive method nor the original 7-element MVDR method is effective in suppressing multiple false targets. This limitation arises from the performance of the original 7-element MVDR method being constrained by the number of physical transmit elements, thereby preventing the suppression of an interference count that exceeds the physical array size. The underperformance of the virtual array nonadaptive method is attributed to the inappropriate design, resulting in false targets merging with the mainlobe and overlapping the true target. Conversely, Figure 14b demonstrates that the virtual array nonadaptive method successfully suppresses multiple false targets and achieves performance close to the ideal performance curve. This is attributed to the effective utilization of virtual DOFs by the designed $\Delta f = f_r\left(z + \frac{i}{pM}\right)$ configuration, surpassing the limitations imposed by the number of physical transmit elements.

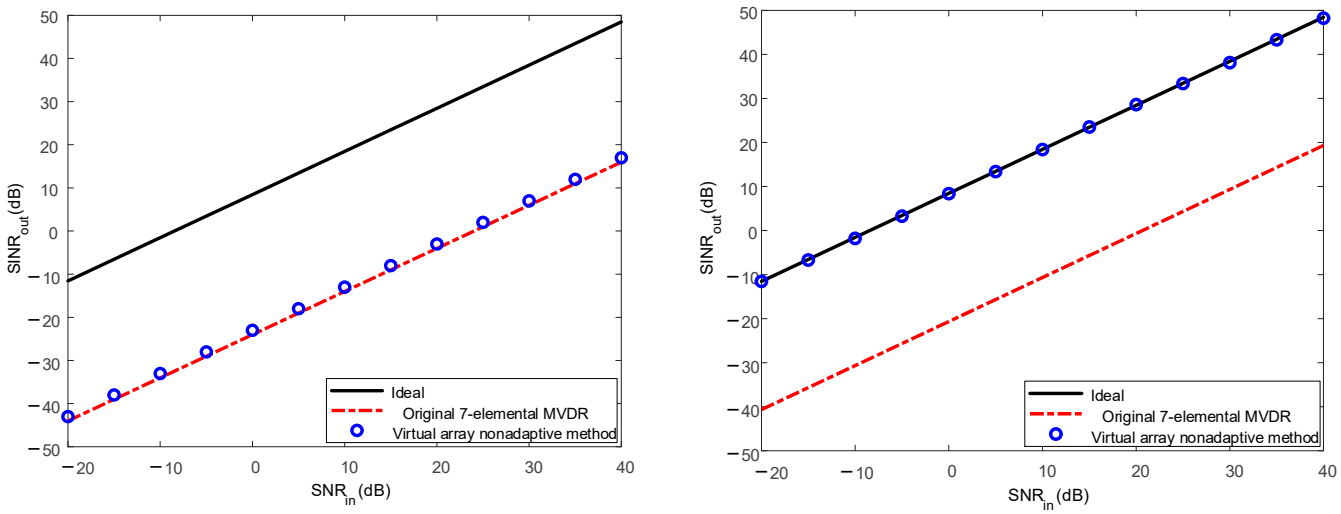

(**a**) (**b**)

Figure 14. The output SINR performance under 14 false targets. (**a**) $\Delta f = f_r\left(z + \frac{i}{pM}\right)$. (**b**) $\Delta f = f_r\left(z + \frac{i}{p(2\mathbb{V}+1)}\right)$.

5. Conclusions

In this work, we have developed a frequency increment Δf for the MR-FDA-MIMO radar system to effectively suppress multiple false targets. The MR-FDA-MIMO radar system employs a ULA at the receive port and leverages the robust MVDR method to effectively suppress sidelobe barrage interference. At the transmit port, a difference co-array is implemented to expand the virtual DOFs, thereby enhancing the resolution capabilities. By appropriately designing a suitable Δf, it becomes possible to tackle the challenge of exceeding the physical element limit for mainlobe deceptive interference. Nonadaptive methods are employed to suppress multiple false targets regardless of the availability of virtual sample data, thereby mitigating the issue of limited virtual sample numbers. Additionally, leveraging system prior knowledge, a nonadaptive beamformer based on a virtual array is designed in such a way that the nulls of the beampattern align with potential mainlobe deceptive interference areas. The simulation results obtained demonstrate the effectiveness of the Δf design based on a virtual array in effectively suppressing multiple mainlobe deceptive interference.

Author Contributions: Formal analysis, Z.W.; methodology, Z.W.; supervision, S.Z., J.X. and X.L.; writing—original draft, Z.W.; writing—review and editing, Z.W., J.X., L.L. and Y.Z. All authors have read and agreed to the published version of the manuscript.

Funding: This research was funded in part by the Nature Science Foundation of China (NSFC) under Grants (Nos. 61931016, 62071344, 62101402), in part by the Natural Science Basic Research Program of Shaanxi (No. 2023-JC-JQ-55), in part by the China Postdoctoral Science Foundation (Nos. 2021TQ0261, 2021M702547), in part by the Innovation Capability Support Program of Shaanxi (No. 2022KJXX-38) and the Science and Technology Innovation Team of Shaanxi Province (NO. 2022TD-38).

Conflicts of Interest: The authors declare no conflict of interest.

References

1. Farina, A. Electronic Counter-Countermeasures. In *Radar Handbook*, 3rd ed.; Skolnik, M., Ed.; McGraw-Hill: New York, NY, USA, 2008; Chapter 24.
2. Yan, L.; Addabbo, P.; Hao, C.; Orlando, D.; Farina, A. New ECCM Techniques against Noiselike and/or Coherent Interferers. *IEEE Trans. Aerosp. Electron. Syst.* **2020**, *56*, 1172–1188. [CrossRef]
3. Soumekh, M. SAR-ECCM using phase-perturbed LFM chirp signals and DRFM repeat jammer penalization. *IEEE Trans. Aerosp. Electron. Syst.* **2006**, *42*, 191–205. [CrossRef]
4. Zoltowski, M. On the performance analysis of the MVDR beamformer in the presence of correlated interference. *IEEE Trans. Acoustic. Speech. Signal Process.* **1988**, *36*, 945–947. [CrossRef]
5. Li, Y.; Jia, X.; Chen, Y.; Yin, C. Frequency agility MIMO-SAR imaging and anti-deception jamming performance. In Proceedings of the 2014 31th URSI General Assembly and Scientific Symposium (URSI GASS), Beijing, China, 16–23 August 2014; pp. 1–4. [CrossRef]
6. Xiong, W.; Zhang, G.; Wen, F.; Zhang, Y.; Yin, J. Trilinear decomposition-based spatial-polarisational filter method for deception jamming suppression of radar. *IET Radar Sonar Navig.* **2016**, *10*, 765–773. [CrossRef]
7. Wen, C.; Huang, Y.; Zheng, L.; Liu, W.; Davidson, T.N. Transmit Waveform Design for Dual-Function Radar-Communication Systems via Hybrid Linear-Nonlinear Precoding. *IEEE Trans. Signal Process.* **2023**, *71*, 2130–2145. [CrossRef]
8. Qian, J.; He, Z. Mainlobe interference suppression with eigenprojection algorithm and similarity constraints. *Electron. Lett.* **2016**, *52*, 228–230. [CrossRef]
9. Zhang, L.; Su, L.; Wang, D.; Luo, Y.; Zhang, Q. Mainlobe Interference Suppression for Radar Network via RPCA-based Covariance Matrix Reconstruction. *IEEE Sens. J.* **2023**, *23*, 5094–5108. [CrossRef]
10. Han, X.; He, H.; Zhang, Q.; Yang, L.; He, Y. Suppression of Deception-False-Target Jamming for Active/Passive Netted Radar Based on Position Error. *IEEE Sens. J.* **2022**, *22*, 7902–7912. [CrossRef]
11. Gao, S.; Yang, X.; Lan, T.; Han, B.; Sun, H.; Yu, Z. Radar main-lobe jamming suppression and identification based on robust whitening Blind Source Separation and Convolutional Neural Networks. *IET Radar Sonar Navig.* **2022**, *16*, 552–563. [CrossRef]
12. Antonik, P. An Investigation of a Frequency Diverse Array. Ph.D. Thesis, University College London, London, UK, 2009.
13. Wang, W.; So, H.C. Transmit Subaperturing for Range and Angle Estimation in Frequency Diverse Array Radar. *IEEE Trans. Signal Process.* **2014**, *62*, 2000–2011. [CrossRef]
14. Baizert, P.; Hale, T.B.; Temple, M.A.; Wicks, M.C. Forward-looking radar GMTI benefits using a linear frequency diverse array. *Electron. Lett.* **2006**, *42*, 1311–1312. [CrossRef]

15. Xu, J.; Liao, G.; Huang, L.; So, H.C. Robust adaptive beamforming for fast-moving target detection with FDA-STAP radar. *IEEE Trans. Signal Process.* **2016**, *65*, 973–984. [CrossRef]
16. Lan, L.; Marino, A.; Aubry, A.; De Maio, A.; Liao, G.; Xu, J.; Zhang, Y. GLRT-based Adaptive Target Detection in FDA-MIMO Radar. *IEEE Trans. Aerosp. Electron. Syst.* **2021**, *57*, 597–613. [CrossRef]
17. Wen, C.; Huang, Y.; Davidson, T.N. Efficient Transceiver Design for MIMO Dual-Function Radar-Communication Systems. *IEEE Trans. Signal Process.* **2023**, *71*, 1786–1801. [CrossRef]
18. Basit, A.; Wang, W.; Wali, S.; Nusenu, S.Y. Transmit beamspace design for FDACMIMO radar with alternating direction method of multipliers. *Signal Process.* **2021**, *180*, 107832. [CrossRef]
19. Sammartino, P.F.; Baker, C.J.; Griffiths, H.D. Frequency diverse MIMO techniques for radar. *IEEE Trans. Aerosp. Electron. Syst.* **2013**, *49*, 201–222. [CrossRef]
20. Wen, C.; Tao, M.; Peng, J.; Wu, J.; Wang, T. Clutter suppression for airborne FDA-MIMO radar using multi-waveform adaptive processing and auxiliary channel STAP. *Signal Process.* **2019**, *154*, 280–293. [CrossRef]
21. Xu, J.; Liao, G.; So, H.C. Space-Time Adaptive Processing With Vertical Frequency Diverse Array for Range-Ambiguous Clutter Suppression. *IEEE Trans. Geosci. Remote Sens.* **2016**, *54*, 5352–5364. [CrossRef]
22. Wang, Y.; Zhu, S.; Lan, L.; Li, X.; Liu, Z.; Wu, Z. Range-Ambiguous Clutter Suppression via FDA MIMO Planar Array Radar with Compressed Sensing. *Remote Sens.* **2022**, *14*, 1926. [CrossRef]
23. Wen, C.; Huang, Y.; Peng, J.; Wu, J.; Zheng, G.; Zhang, Y. Slow-Time FDA-MIMO Technique With Application to STAP Radar. *IEEE Trans. Aerosp. Electron. Syst.* **2022**, *58*, 74–95. [CrossRef]
24. Xu, J.; Liao, G.; Zhu, S.; So, H.C. Deceptive jamming suppression with frequency diverse MIMO radar. *Signal Process.* **2015**, *113*, 9–17. [CrossRef]
25. Ding, Z.; Xie, J.; Xu, J. A Joint Array Parameters Design Method Based on FDA-MIMO Radar. *IEEE Trans. Aerosp. Electron. Syst.* **2023**, *59*, 2909–2919. [CrossRef]
26. Zhang, Y.; Liao, G.; Xu, J.; Lan, L. Mainlobe Deceptive Jammer Suppression Based on Quadratic Phase Coding in FDA-MIMO Radar. *Remote Sens.* **2022**, *14*, 5831. [CrossRef]
27. Nysaeter, A. Adaptive suppression of smart jamming with FDA permutation. In Proceedings of the 2022 IEEE Radar Conference (RadarConf22), New York, NY, USA, 21–25 March 2022; pp. 1–5. [CrossRef]
28. Tan, M.; Wang, C.; Xue, B.; Xu, J. A novel deceptive jamming approach against frequency diverse array radar. *IEEE Sens. J.* **2021**, *21*, 8323–8332. [CrossRef]
29. Lan, L.; Xu, J.; Liao, G.; Zhang, Y.; Fioranelli, F.; So, H.C. Suppression of Mainbeam Deceptive Jammer With FDA-MIMO Radar. *IEEE Trans. Veh. Technol.* **2020**, *69*, 11584–11598. [CrossRef]
30. Zhang, X.; Cao, D.; Xu, L. Joint polarisation and frequency diversity for deceptive jamming suppression in MIMO radar. *IET Radar Sonar Navig.* **2019**, *13*, 263–271. [CrossRef]
31. Jia, W.; Wang, W.; Zhang, S. Joint design of the transmit and receive weights for coherent FDA radar. *Signal Process.* **2023**, *204*, 108834. [CrossRef]
32. Moffet, A. Minimum-redundancy linear arrays. *IEEE Trans. Antenna. Propaga.* **1968**, *16*, 172–175. [CrossRef]
33. Pal, P.; Vaidyanathan, P. Multiple level nested array: An efficient geometry for 2qth order cumulate based array processing. *IEEE Trans. Signal Process.* **2012**, *60*, 1253–1269. [CrossRef]
34. Vaidyanathan, P.P.; Pal, P. Sparse sensing with co-prime samplers and arrays. *IEEE Trans. Signal Process.* **2011**, *59*, 573–586. [CrossRef]
35. Wen, C.; Huang, Y.; Peng, J.; Zheng, G.; Liu, W.; Zhang, J. Reconfigurable Sparse Array Synthesis With Phase-Only Control via Consensus-ADMM-Based Sparse Optimization. *IEEE Trans. Veh. Technol.* **2021**, *70*, 6647–6661. [CrossRef]
36. Zheng, Z.; Yang, C.; Wang, W.; So, H. Robust DOA Estimation Against Mutual Coupling With Nested Array. *IEEE Signal Process. Lett.* **2020**, *27*, 1360–1364. [CrossRef]
37. Zheng, Z.; Huang, Y.; Wang, W.; So, H. Direction-of-Arrival Estimation of Coherent Signals via Coprime Array Interpolation. *IEEE Signal Process. Lett.* **2020**, *27*, 585–589. [CrossRef]
38. Pal, P.; Vaidyanathan, P. Nested Arrays in Two Dimensions, Part II: Application in Two Dimensional Array Processing. *IEEE Trans. Signal Process.* **2012**, *60*, 4706–4718. [CrossRef]
39. Wang, C.; Zhang, X.; Li, J. FDA-MIMO radar for 3D localization: Virtual coprime planar array with unfolded coprime frequency offset framework and TRD-MUSIC algorithm. *Digit. Signal Process.* **2021**, *113*, 103017. [CrossRef]
40. Qin, S.; Zhang, Y.; Amin, M.; Gini, F. Frequency diverse coprime arrays with coprime frequency offsets for multitarget localization. *IEEE J. Sel. Top. Signal Process.* **2017**, *11*, 321–335. [CrossRef]
41. Wang, X.; Yang, Z.; Huang, J.; Lamare, R. Robust Two-Stage Reduced-Dimension Sparsity-Aware STAP for Airborne Radar With Coprime Arrays. *IEEE Trans. Signal Process.* **2020**, *68*, 81–96. [CrossRef]
42. Shi, J.; Xie, L.; Cheng, Z.; He, Z.; Zhang, W. Angle-Doppler Channel Selection Method for Reduced-Dimension STAP Based on Sequential Convex Programming. *IEEE Commun. Lett.* **2021**, *25*, 3080–3084. [CrossRef]
43. Duan, H.; Ng, B.P.; See, C.M.S.; Fang, J. Broadband interference suppression performance of minimum redundancy arrays. *IEEE Trans. Signal Process.* **2008**, *56*, 2406–2416. [CrossRef]
44. Yang, J.; Liao, G.; Li, J. Robust adaptive beamforming in nested array. *Signal Process.* **2015**, *114*, 143–149. [CrossRef]

45. Zhou, C.; Gu, Y.; He, S.; Shi, Z. A Robust and Efficient Algorithm for Coprime Array Adaptive Beamforming. *IEEE Trans. Veh. Technol.* **2018**, *67*, 1099–1112. [CrossRef]
46. Wu, Z.; Zhu, S.; Xu, J.; Lan, L.; Li, X. FDA-MRMO Radar Interference Suppression. In Proceedings of the 2022 IEEE International Symposium on Phased Array Systems & Technology (PAST), Waltham, MA, USA, 11–14 October 2022; pp. 1–6. [CrossRef]
47. Wu, Z.; Zhu, S.; Xu, J.; Lan, L.; Zhang, M. Interference Suppression Method with MR-FDA-MIMO Radar. *IEEE Trans. Aerosp. Electron. Syst.* **2023**. [CrossRef]
48. Xu, J.; Liao, G.; Zhu, S.; Huang, L.; So, H.C. Joint range and angle estimation using MIMO radar with frequency diverse array. *IEEE Trans. Signal Process.* **2015**, *63*, 3396–3410. [CrossRef]
49. Xu, J.; Liao, G.; Zhang, Y.; Ji, H.; Huang, L. An adaptive range-angle-Doppler processing approach for FDA-MIMO radar using three-dimensional localization. *IEEE J. Sel. Top. Signal Process.* **2017**, *11*, 309–320. [CrossRef]
50. Lan, L.; Liao, G.; Xu, J.; Xu, Y.; So, C. Beampattern Synthesis Based on Novel Receive Delay Array for Mainlobe Interference Mitigation. *IEEE Trans. Antennas Propag.* **2023**, *71*, 4470–4485. [CrossRef]
51. Lan, L.; Liao, G.; Xu, J.; Zhang, Y.; Fioranelli, F. Suppression approach to main-beam deceptive jamming in FDA-MIMO radar using nonhomogeneous sample detection. *IEEE Access* **2018**, *6*, 34582–34597. [CrossRef]
52. Ahmed, S. Product-based pulse integration to combat noise jamming. *IEEE Trans. Aerosp. Electron. Syst.* **2014**, *50*, 2109–2115. [CrossRef]
53. Gu, Y.; Leshem, A. Robust Adaptive Beamforming Based on Interference Covariance Matrix Reconstruction and Steering Vector Estimation. *IEEE Trans. Signal Process.* **2012**, *60*, 3881–3885. [CrossRef]
54. Lan, L.; Liao, G.; Xu, J.; Zhang, Y.; Liao, B. Transceive beamforming with accurate nulling in FDA-MIMO radar for imaging. *IEEE Trans. Geosci. Remote Sens.* **2020**, *58*, 4145–4159. [CrossRef]
55. Pal, P.; Vaidyanathan, P. Nested Arrays: A Novel Approach to Array Processing With Enhanced Degrees of Freedom. *IEEE Trans. Signal Process.* **2010**, *58*, 4167–4181. [CrossRef]
56. Reed, I.; Mallett, J.; Brennan, L. Rapid convergence rate in adaptive arrays. *IEEE Trans. Aerosp. Electron. Syst.* **1974**, *10*, 853–863. [CrossRef]